Wrench Estimation and Impedance-based Control applied to a Flying Parallel Robot Interacting with the Environment

Shiyu Liu, Isabelle Fantoni, Abdelhamid Chriette, Damien Six

Wrench Estimation and Impedance-based Control applied to a Flying Parallel Robot Interacting with the Environment

Shiyu Liu * **Isabelle Fantoni** ** **Abdelhamid Chriette** * **Damien Six** *

* *Ecole Centrale de Nantes, Laboratoire des Sciences du Numérique de Nantes (LS2N), 1 Rue de la Noë, 44321 Nantes, France (e-mails: {shiyu.liu, abdelhamid.chriette, damien.six}@ls2n.fr).*
** *Centre National de la Recherche Scientifique, LS2N, 1 Rue de la Noë, 44321 Nantes, France (e-mail: isabelle.fantoni@ls2n.fr).*

Abstract: Multi-vehicle aerial robots present great potential in accomplishing manipulation tasks, because of their high payload capacity and full manipulability in 3-dimensional space. Belonging to this class of aerial robots, the Flying Parallel Robot (FPR) is an architecture where a moving platform is supported collectively by a team of quadrotors with passive kinematic chains. While the modelling and control of the FPR in free space has been studied in the previous work, there is lack of consideration in robot-environment interaction, which is however significant to develop the industrial applications of such robots. In this paper, we implement an external wrench estimator and an impedance-based controller with force tracking capability to achieve the disturbance rejection and the physical interaction with the environment. Extensive experimental validations have shown the FPR capable of hovering in presence of additional payload and strong wind perturbations, and performing contact-based interaction tasks.

Keywords: Aerial Systems: Mechanics and Control, Impedance Control, Multi-vehicle Systems

1. INTRODUCTION

The aerial vehicles and their applications to aerial manipulation have been intensively studied in the last decade. Unmanned aerial vehicles (UAVs) are typically equipped with robotic arms or other end-effectors for performing tasks at locations inaccessible or very dangerous for human operators (Ollero et al., 2021). More recently, designs based on a parallel mechanical architecture have been proposed where a moving platform (or a payload) is collectively supported by multiple UAVs using cables (Michael et al., 2011; Sanalitro et al., 2020) or rigid links (Nguyen et al., 2018; Li et al., 2021; Six et al., 2018). Such robots have shown their potential in accomplishing various manipulation tasks due to higher payload capacity and better manipulability, which might largely extend the application fields of the flying robots.

Belonging to the class of multi-UAV parallel robots, the Flying Parallel Robot (FPR) initially proposed by Six et al. (2018) is a design where multiple UAVs are associated to a rigid articulated architecture to support a moving platform collectively. As an analogy to the parallel mechanism, the FPR can drive the platform with better mobility in particular the rotational movements by additional degrees of freedom (DoFs) in passive kinematic chains. The previous works in Six et al. (2018); Liu et al. (2021) have shown that by proper modelling and motion controller design, a stable flight in ideally unperturbed environment on autopilot or by teleoperation is achievable. However, the FPR working in more complex situations must be investigated especially considering significant interactions with the environment to develop its industrial merits for potential application scenarios such as infrastructure maintenance and replacement at remote locations.

For aerial robots, the physical interaction with the environment is often challenging as they can easily suffer from other aerodynamic disturbances and uncertainties. Such unknown effects from external environment can generally be handled by two classes of approaches in order to stably control the aerial robots: either by estimating the external effects as in Ruggiero et al. (2014); Tomić et al. (2017)) or via robust control as in Nguyen et al. (2018); Zhang et al. (2019); Sanalitro et al. (2020). The latter strategy assumes that the external disturbances are bounded, which is however not always true in significant robot-environment interactions. With knowledge of external wrench reconstructed by estimation techniques, a reaction behavior of the aerial robots can be designed and thus controlled using force control strategies such as hybrid force/position control (Tzoumanikas et al., 2020), admittance control (Ryll et al., 2019) and impedance control (Bodie et al., 2019). In contrast to hybrid force/position control and admittance control which design an active behavior of the robot and require a considerably precise motion control loop, multi-UAV parallel robots under impedance control reacting passively to the external effects would be more robust especially for interacting significantly with environments.

Shiyu Liu is the corresponding author.
Video of experiments: https://youtu.be/ryffKG-VG68

In this paper, the main contribution is the adaptation and implementation of wrench estimation and impedance-based control techniques to a multi-vehicle aerial robot to achieve the disturbance rejection and the interaction tasks. We then show the effectiveness of the implemented estimation and control methods through extensive experimental validations, including in particular:

- a hovering flight with an additional payload as disturbance performed by several controllers along with the external wrench estimator.
- an analysis on the impedance controller using different impedance gains in presence of external wind perturbations.
- various contact-based interaction tasks performed by the FPR using the wrench estimation and impedance control methods.

The rest of the paper is structured as follows: we begin by presenting the modelling of the FPR in Section 2. A momentum-based external wrench estimator and an impedance-based controller are respectively presented in Section 3 and 4. The experimental results are detailed in Section 5. Finally, the conclusion and potential extensions of this work are discussed in Section 6.

2. MODELLING

The modelling of the FPR is initially presented in Six et al. (2018) and Liu et al. (2021). We reformulate the dynamic model by taking into account the external wrench term.

2.1 System Description

As shown in Fig. 1, the FPR is composed of a moving platform, a number of quadrotors and associated rigid legs, with the number being chosen to 3. Quadrotors are attached to the leg tips by spherical joints and the other ends of legs are connected to the platform by revolute joints. The attached point between each quadrotor and the leg is assumed to be located at the quadrotor's center of mass (CoM), which is also the center of the spherical joint. Therefore, a decoupling between the dynamics of the FPR and the rotational dynamics of quadrotors is ensured by the mechanical properties of spherical joints, allowing to consider the quadrotors as rotating thrust generators in 3-dimensional space.

Let $\mathcal{F}_0(O, x, y, z)$ denote a global inertial reference frame, $\mathcal{F}_p(O_p, x_p, y_p, z_p)$ be the platform frame attached to its CoM. $\mathcal{F}_{li}(O_{li}, x_{li}, y_{li}, z_{li})$ is the leg i's frame placed at the center of the revolute joint and $\mathcal{F}_{bi}(O_{bi}, x_{bi}, y_{bi}, z_{bi})$ is the quadrotor i's body frame placed at the quadrotor's CoM. $i = \{1, 2, 3\}$ is an index of the number of quadrotor/leg which remains the same in the rest of the paper. An end-effector can be mounted on the platform and has its own frame, assumed to be aligned with the platform frame $\mathcal{F}_p$.

We denote $\mathbf{p}_p \in \mathbb{R}^3$, $\mathbf{h}_p \in \mathbb{H}$ as the position and the orientation of the platform with respect to $\mathcal{F}_0$. The orientation $\mathbf{h}_p$ is represented by a unit quaternion, with $\mathbb{H}$ being the quaternion space. $\boldsymbol{\theta}_l = [\theta_{l1}, \theta_{l2}, \theta_{l3}]^T \in \mathbb{R}^3$ is denoted as a vector of the included angles between the platform plane and each leg's direction. The generalized coordinates of the FPR is thus given by

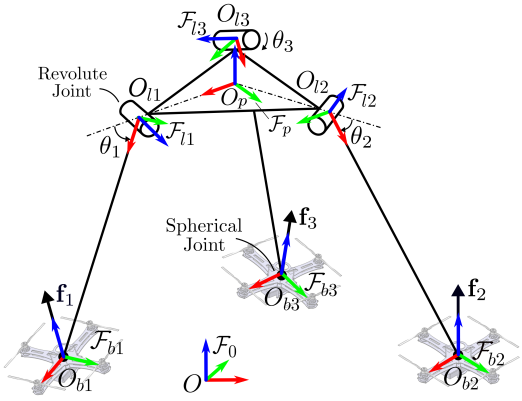

Fig. 1. General scheme of the FPR

$$\mathbf{q} = [\mathbf{p}_p^T,\ \mathbf{h}_p^T,\ \boldsymbol{\theta}_l^T]^T \in \mathbb{R}^{10} \tag{1}$$

The generalized velocity of the FPR is defined by

$$\boldsymbol{\nu} = [\mathbf{v}_p^T,\ {}^p\boldsymbol{\omega}_p^T,\ \dot{\boldsymbol{\theta}}_l^T]^T \in \mathbb{R}^9 \tag{2}$$

where $\mathbf{v}_p$ is the linear velocity of the platform expressed in $\mathcal{F}_0$, ${}^p\boldsymbol{\omega}_p$ is the body-frame angular velocity of the platform and $\dot{\boldsymbol{\theta}}_l$ is a vector of the leg angle rates.

2.2 Kinematics

The inverse kinematic model (IKM) of the FPR links the generalized velocity vector to the linear velocities of the quadrotors. Let $\mathbf{v} = [\mathbf{v}_1^T, \mathbf{v}_2^T, \mathbf{v}_3^T]^T \in \mathbb{R}^9$ be a vector including the linear velocities of three quadrotors, with $\mathbf{v}_i \in \mathbb{R}^3$ being quadrotor i's linear velocity expressed in $\mathcal{F}_0$. The IKM is written by

$$\mathbf{v} = \mathbf{J}(\mathbf{q})\boldsymbol{\nu} \tag{3}$$

where $\mathbf{J}(\mathbf{q}) \in \mathbb{R}^{9\times 9}$ is the Jacobian matrix derived from the geometric relationship. The forward kinematic model (FKM) is then defined by the inverse problem of (3) as

$$\boldsymbol{\nu} = \mathbf{J}(\mathbf{q})^{-1}\mathbf{v} \tag{4}$$

supposing that $\det(\mathbf{J}) \neq 0$, i.e. the robot is always working in non-singular configurations. Based on the singularity analysis detailed in Six et al. (2018), this assumption holds true as long as the leg angles are all restricted within the range of $[0, \pi/2]$.

2.3 Dynamics

We denote the robot input (i.e. thrust forces of the quadrotors) by a vector $\mathbf{f} = [\mathbf{f}_1^T, \mathbf{f}_2^T, \mathbf{f}_3^T]^T \in \mathbb{R}^9$ with $\mathbf{f}_i$ representing quadrotor i's 3-dimensional thrust force expressed in $\mathcal{F}_0$. The dynamics of the FPR can be derived in matrix form taking into account the external wrench term as

$$\mathbf{M}(\mathbf{q})\dot{\boldsymbol{\nu}} + \mathbf{C}(\mathbf{q}, \boldsymbol{\nu})\boldsymbol{\nu} + \mathbf{g}(\mathbf{q}) = \mathbf{J}(\mathbf{q})^T\mathbf{f} + \boldsymbol{\tau}_e \tag{5}$$

where $\mathbf{M}(\mathbf{q}) \in \mathbb{R}^{9\times 9}$ is the generalized inertia matrix, $\mathbf{C}(\mathbf{q}, \boldsymbol{\nu}) \in \mathbb{R}^{9\times 9}$ is the Coriolis matrix factorizing the Coriolis and centrifugal terms, $\mathbf{g}(\mathbf{q}) \in \mathbb{R}^9$ is the vector of gravitational effects, and $\boldsymbol{\tau}_e = [\mathbf{f}_{p,e}^T, {}^p\mathbf{m}_{p,e}^T, \mathbf{m}_{l,e}^T]^T \in \mathbb{R}^9$ denotes the external wrench acting on the FPR, with $\mathbf{f}_{p,e}$ being the 3-dimensional force expressed in $\mathcal{F}_0$, ${}^p\mathbf{m}_{p,e}$ the 3-dimensional moment in $\mathcal{F}_p$, which are exerted on the platform, and $\mathbf{m}_{l,e} = [m_{l1}, m_{l2}, m_{l3}]_e^T \in \mathbb{R}^3$ representing the external moments about the revolute joints of the legs.

3. EXTERNAL WRENCH ESTIMATION

Knowing the system input $\mathbf{f}$ and the response of the robot states (i.e. $\mathbf{q}$ and $\boldsymbol{\nu}$), the dynamic model presented in Section 2 can be used to estimate the external wrench $\boldsymbol{\tau}_e$ acting on the robot. We apply a momentum-based wrench estimator to reconstruct this unknown information.

3.1 Momentum-based Wrench Estimation

Given the generalized inertia matrix $\mathbf{M}$ computed by the dynamic model, the generalized momentum vector of the FPR can be defined as

$$\boldsymbol{\mathcal{P}} = \mathbf{M}(\mathbf{q})\boldsymbol{\nu} \ \in \mathbb{R}^9 \tag{6}$$

From the properties of dynamic systems as detailed in Echeandia and Wensing (2021), the following expression can be proven

$$\dot{\mathbf{M}}(\mathbf{q}) = \mathbf{C}(\mathbf{q}, \boldsymbol{\nu}) + \mathbf{C}(\mathbf{q}, \boldsymbol{\nu})^T \tag{7}$$

Based on (5) and (7), the time derivative of the generalized momentum is

$$\dot{\boldsymbol{\mathcal{P}}} = \mathbf{C}(\mathbf{q}, \boldsymbol{\nu})^T\boldsymbol{\nu} - \mathbf{g}(\mathbf{q}) + \mathbf{J}(\mathbf{q})^T\mathbf{f} + \boldsymbol{\tau}_e \tag{8}$$

from which the external wrench $\boldsymbol{\tau}_e$ can be directly computed. However, the measurements of the robot state might be too noisy to construct a stable estimation. Therefore, we apply a first-order filtering on the estimation by

$$\dot{\hat{\boldsymbol{\tau}}}_e = \mathbf{K}_\tau(\boldsymbol{\tau}_e - \hat{\boldsymbol{\tau}}_e) \tag{9}$$

By integrating (9) and using (8), the estimate of the external wrench is given by

$$\begin{aligned}\hat{\boldsymbol{\tau}}_e(t) = \mathbf{K}_\tau \Bigg[\boldsymbol{\mathcal{P}}(t) - \int_{t_0}^{t} \Big(&\mathbf{C}(\mathbf{q}, \boldsymbol{\nu})^T\boldsymbol{\nu} - \mathbf{g}(\mathbf{q}) \\ &+ \mathbf{J}(\mathbf{q})^T\mathbf{f} + \hat{\boldsymbol{\tau}}_e(t-\delta t)\Big)dt - \boldsymbol{\mathcal{P}}(t_0)\Bigg]\end{aligned} \tag{10}$$

where $\boldsymbol{\mathcal{P}}(t_0)$ is the momentum at initial time, which is zero supposing that $\boldsymbol{\nu}(t_0) = \mathbf{0}$, $\mathbf{K}_\tau \in \mathbb{R}^{9\times9}$ is a positive-definite diagonal matrix as the estimation gains. We remark that the current estimate of the external wrench $\hat{\boldsymbol{\tau}}_e(t)$ depends on the previous estimate $\hat{\boldsymbol{\tau}}_e(t-\delta t)$. As the algorithm is implemented in discrete time, the estimator simply uses the last estimate to perform the following step of estimation with $\hat{\boldsymbol{\tau}}_e(t_0)$ initialized by zero.

3.2 Contact Force Determination

During a contact between the platform and an object in the environment, the platform (or the attached end-effector) exerts a certain amount of force along its normal direction, i.e. z axis of the platform frame $\mathcal{F}_p$. The reaction force exerted on the platform due to the interaction with the environment is thus estimated by $\hat{\mathbf{f}}_{p,e}$, which is initially expressed in global frame $\mathcal{F}_0$. It can then be expressed in $\mathcal{F}_p$ by ${}^p\hat{\mathbf{f}}_{p,e} = \mathbf{R}_p^T\hat{\mathbf{f}}_{p,e}$ given the rotation matrix $\mathbf{R}_p$ associated with the actual orientation of the platform. This allows us to determine the contact force with the environment along the normal direction of the platform plane by ${}^p\hat{f}_{p_z,e}$, i.e. z-axis component of ${}^p\hat{\mathbf{f}}_{p,e}$. This variable represents the contact force the environment exerts on the platform, and its negative value is the force the platform pushes to the external environment.

3.3 Discussion and Practical Considerations

We hereby discuss the implementation and practical concerns of applying this momentum-based estimator to reconstruct the external wrench using the dynamic model. The Spatial Vector-based algorithm is used to accelerate the on-line computation of the dynamic model. A numerical algorithm proposed in Echeandia and Wensing (2021) is furthermore applied to compute the Coriolis matrix, which can also be done by any other admissible factorization methods.

To perform the estimation, only knowledge of the current configuration and velocity of the FPR is necessary, with the former measured by the Motion Capture system and the latter computed by the FKM in (4) using measurements of the linear velocities of the quadrotors. This computed velocity of the FPR is supposed precise enough with an accurate kinematic model as the linear velocities of quadrotors are commonly well filtered onboard using techniques such as Extended Kalman Filter (EKF). However, equation (10) assumes that the thrust force commands $\mathbf{f}$ are well achieved by the quadrotors for an unbiased estimation, which however cannot be always ensured in practical cases. Therefore, the uncertainties on thrust forces generated by quadrotors will also be present in the external wrench estimates. We suppose that this factor is small enough to be neglected compared to other disturbances or interactions with the environment.

4. IMPEDANCE-BASED INTERACTION CONTROL

Having shown that the external wrench can be reconstructed by accessible robot states, we now consider how to better control the FPR to interact with the environment. While the admittance control approach is commonly seen in tackling interactions as in Ryll et al. (2019) because of its implementation simplicity, it is difficult to select the gains to obtain an appropriate interaction behavior and more importantly, admittance controller requires a considerably precise motion control loop which itself is not evident for multi-vehicle aerial robots. In contrast, the impedance control approach regulates the interaction wrench by a virtual mass-spring-damper system, controlling directly the interaction behavior and replacing the existing motion control of the flying robots. Furthermore, the impedance controller can be used to both reject the disturbance and perform the interaction task, with no need of switching controllers as required in hybrid position/force control. We implement an impedance-based controller with force tracking capability applying the wrench estimator presented in Section 3. A block diagram of the complete estimation and control framework is shown in Fig. 2.

4.1 Impedance Control Formulation

Let $\mathbf{q}^d, \boldsymbol{\nu}^d, \dot{\boldsymbol{\nu}}^d$ be the desired position, velocity and acceleration coordinates of the robot, respectively. A generalized form of the desired dynamic behavior of the robot can be chosen as

$$\mathbf{M}^d(\dot{\boldsymbol{\nu}}^d - \dot{\boldsymbol{\nu}}) + \mathbf{B}^d(\boldsymbol{\nu}^d - \boldsymbol{\nu}) + \mathbf{K}^d\boldsymbol{\varepsilon}_q(\mathbf{q}^d, \mathbf{q}) = \boldsymbol{\varepsilon}_\tau \tag{11}$$

where $\mathbf{M}^d$, $\mathbf{B}^d$ and $\mathbf{K}^d \in \mathbb{R}^{9\times9}$ are the positive-definite diagonal matrices respectively for the desired mass, damping and stiffness coefficients of the system, which are

decoupled on each robot state. The input of the desired impedance system is defined to be the wrench tracking error $\boldsymbol{\varepsilon}_\tau$ as in Seraji and Colbaugh (1997), which is calculated by $\boldsymbol{\varepsilon}_\tau = -\hat{\boldsymbol{\tau}}_e - \boldsymbol{\tau}_e^d \in \mathbb{R}^9$, with $-\hat{\boldsymbol{\tau}}_e$ being the estimated interaction wrench the robot exerts on the environment and $\boldsymbol{\tau}_e^d$ representing the desired interaction wrench. $\boldsymbol{\varepsilon}_q(\mathbf{q}^d, \mathbf{q})$ is the tracking error of the robot configuration, in which the platform orientation error is computed by the quaternion error between the desired and actual orientations as in Brescianini et al. (2013).

Based on (11), we introduce an auxiliary input $\mathbf{u} = \dot{\boldsymbol{\nu}}$ corresponding to the acceleration of the robot by

$$\mathbf{u} = \dot{\boldsymbol{\nu}}^d + (\mathbf{M}^d)^{-1}\left[\mathbf{B}^d(\boldsymbol{\nu}^d - \boldsymbol{\nu}) + \mathbf{K}^d\boldsymbol{\varepsilon}_q(\mathbf{q}^d, \mathbf{q}) - \boldsymbol{\varepsilon}_\tau\right] \quad (12)$$

The system input can then be calculated by linearization using the dynamic model of (5) as

$$\mathbf{f} = \mathbf{J}(\mathbf{q})^{-T}\left[\mathbf{M}(\mathbf{q})\mathbf{u} + \mathbf{C}(\mathbf{q}, \boldsymbol{\nu})\boldsymbol{\nu} + \mathbf{g}(\mathbf{q}) - \hat{\boldsymbol{\tau}}_e\right] \quad (13)$$

with $\hat{\boldsymbol{\tau}}_e$ being the external wrench estimates calculated by (10). According to Ruggiero et al. (2014), the stability of the impedance controlled system with external wrench estimation can be ensured if the estimation error, i.e. $\boldsymbol{\tau}_e - \hat{\boldsymbol{\tau}}_e$, is bounded. Furthermore, the time-scale separation argument commonly found in several robotics applications are exploited dealing with feedback control with estimation. The estimator dynamics are supposed fast enough such that its transient behavior can be considered as a bounded perturbation with respect to the robot motion.

4.2 Quadrotor Control

Once the control input $\mathbf{f}$ is computed, we can calculate the commands sent to the quadrotors, composed of desired thrust magnitude $f_i^d \in \mathbb{R}$ and desired attitude $\mathbf{h}_i^d \in \mathbb{H}$ for each quadrotor i. The desired thrust magnitude is calculated by the norm of the corresponding thrust force vector (i.e. $f_i^d = \|\mathbf{f}_i\|$). For the desired attitude, the desired z axis of $\mathcal{F}_{bi}$ is directly determined by $z_{bi}^d = \mathbf{f}_i/\|\mathbf{f}_i\|$. The desired x axis of $\mathcal{F}_{bi}$ is then defined with a constant angle relative to the leg i's direction on the plane perpendicular to z_{bi}^d, in purpose of avoiding potential collisions between propellers and the leg. Therefore, the rotation matrix defining quadrotor i's attitude can be determined by $\mathbf{R}_{bi}^d = [x_{bi}^d \;\; z_{bi}^d \times x_{bi}^d \;\; z_{bi}^d]$, which is further converted to $\mathbf{h}_i^d$.

The onboard controller of each quadrotor tracks the thrust and attitude setpoints using a controller such as Brescianini et al. (2013). We suppose that quadrotors can well perform the attitude tracking with rapid convergence as the response of quadrotor rotational dynamics is much faster than that of the FPR dynamics.

4.3 Desired Wrench Determination

The determination of the desired wrench $\boldsymbol{\tau}_e^d$ the robot exerts to the environment depends on the specific task. We hereby control the contact force along z axis in $\mathcal{F}_p$ when the platform interacts with the environment. The desired force is thus chosen to be ${}^p\mathbf{f}_{p,e}^d = [0, 0, f_{p_z,e}^d]^T$, with $f_{p_z,e}^d$ being the desired contact force between the platform and the environment along the normal direction of the platform. This desired contact force is converted to be expressed in $\mathcal{F}_0$ by $\mathbf{f}_{p,e}^d = \mathbf{R}_p\,{}^p\mathbf{f}_{p,e}^d$, which is then used to calculate the force tracking error. The rest of the elements in $\boldsymbol{\tau}_e^d$ is set to zero, resulting in a compliance behavior to the disturbances acting on those axes.

4.4 Discussion on Impedance Tuning

The impedance gains in (11) are determined on the basis of the desired impedance behavior for the robot-environment interaction, which are tuned according to the specific interaction task. For instance, a high stiffness is chosen to reject disturbances in performing a steady flight, while a lower value will be more appropriate to ensure the compliance behavior of the robot during the interaction tasks. On the other hand, the mass and damping coefficients must be properly defined to avoid overshooting and oscillations. Furthermore, the damping ratio of the desired impedance system can be taken into account, which is calculated by

$$\zeta = \frac{\mathrm{B}^d}{2\sqrt{\mathrm{K}^d\mathrm{M}^d}} \quad (14)$$

The system is under-damped when $\zeta < 1$, critically damped when $\zeta = 1$, and over-damped when $\zeta > 1$. The damping ratio is usually selected between 0.4 and 0.7 in general case (Shinners, 1998).

In practical case, the impedance gains are pre-tuned to allow the FPR to achieve a steady flight in free space and can be varied according to the different application scenarios. We select a small damping ratio for the platform position state to have a rapid response to the environmental effects. A slightly under-damped behavior of the platform's rotational movement is chosen to reach the best trade-off between the response time and the acceptable overshoot. In contrast, an over-damped behavior on the leg angle states is preferred such that overshooting and sensibility to external disturbances are limited, which is beneficial to the FPR for both being away from singular configurations and maintaining the wrench capability during the interaction tasks.

5. EXPERIMENTAL RESULTS

In this section, we present the experimental results which validate the wrench estimation and impedance control techniques for the disturbance rejection and contact-based interaction tasks. A video of the experiments and the results can be found in https://youtu.be/ryffKG-VG68.

5.1 Experimental Setup

The FPR prototype is shown in Fig. 3 and Fig. 6. The triangle-form platform weights 285 g with side lengths of 20.3 cm. The legs are each 1.05 m long with a mass of 66 g. The custom quadrotors we use are based on a 34 cm Lynxmotion Crazy2Fly frame, with SunnySky 1250kV brushless DC motors, 8045 dual-blade propellers and a 3-cell LiPo battery, weighting totally about 1 kg.

The onboard controllers of the quadrotors are achieved by Pixhawk 4 Mini autopilot with a custom-built PX4 firmware, which are experimentally tuned with aggressive attitude and attitude rate gains to ensure a rapid convergence to the attitude commands. The Raspberry Pi 4B

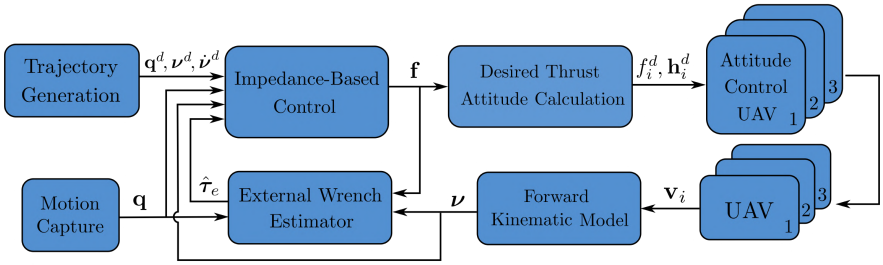

Fig. 2. Block diagram of the external wrench estimation and impedance-based control framework applied to the FPR.

Table 1. Wrench estimation and impedance control gains, and the corresponding damping ratio of the desired impedance system.

	Estimation	Impedance Control			
Robot State	K_τ	M^d	B^d	K^d	ζ
Platform position	2	5	10	25	0.45
Platform orientation	1	8	25	25	0.88
Leg angles	1	5	20	15	1.15

computers are mounted on the quadrotors, handling the communication with the Pixhawk by microRTPS protocol. The wrench estimator and the impedance controller are implemented on a ground computer, with the estimation and control gains given in Table 1. The communications between the ground and onboard computers are handled by ROS2 Galactic, via a 5 GHz Wifi network.

The FPR was flown in a enclosed $4 \times 6 \times 3.5$ m flight arena equipped with an 8-camera Qualisys Motion Capture (MOCAP) system. The MOCAP measures the poses of all the bodies and streams the data over the Wifi network at 100 Hz. The wrench estimator and controller are both run at 50 Hz, and the onboard attitude controller at 250 Hz.

5.2 Experiment I: hovering with an additional payload

In the first experiment, we flew the FPR to perform a hovering flight during 45 s in addition of a 300 g payload attached at the center of the platform, acting as a constant disturbance of about 3 N along negative z axis in the global frame. We performed the same hovering flight using three different controllers: 1) a previously well-tuned PD controller presented in Six et al. (2018); 2) the PD controller with feed-forward external wrench compensation term (named as PD+C controller); 3) the impedance controller with the external wrench estimates. Note that for all the flights, the wrench estimator was activated to construct the external wrench. While it is normal to expect a worse performance by the PD controller, we still performed it simply for a worst case reference.

Fig. 4 shows the results of the tracking of platform's z position, and the estimated external force along z axis in $\mathcal{F}_0$. The root-mean-square errors (RMSE) of the tracking of the other states and the external force estimation is presented in Table 2. From the results, we can conclude that the impedance controller can better deal with unknown disturbances, with a good compliance behavior shown in platform's z position. In addition, the effectiveness of the wrench estimator is validated as the RMSE of the z-axis external force estimates are all about 1 N in three different controllers, which is an acceptable value especially taking into account the large estimation errors in take-off and

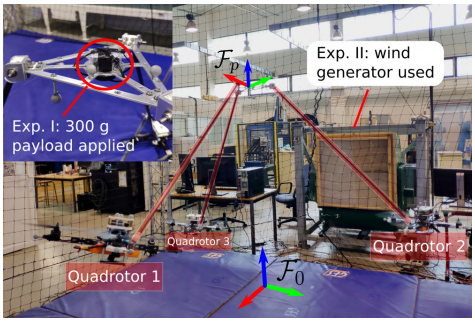

Fig. 3. FPR hovering with an additional payload in Experiment I and in presence of external winds in Experiment II.

landing phases due to the ground effects (during the time interval within [0,2] s and [45,47] s shown in Fig. 4).

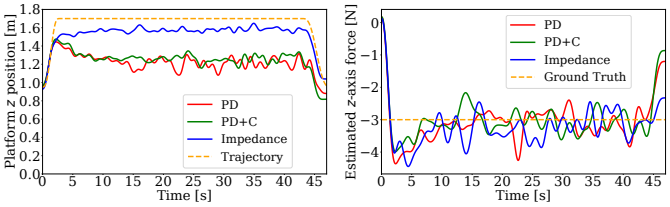

Fig. 4. Comparison of the PD, PD+C, and impedance controllers with external wrench estimates in Experiment I. The left graph presents the tracking of platform's z position and the right graph shows the z-axis external force estimates in the global frame.

Table 2. Root-mean-square error (RMSE) of the trajectory tracking and the z-axis external force estimation in Experiment I. Note that RMSE for $\mathbf{p}_{p,xy}$ refers to the platform positioning error on its x and y axes, ϕ_p and ϑ_p represent the roll and pitch Euler angles of the platform, and RMSE for $\boldsymbol{\theta}_l$ is the mean value of RMSE of three leg angles.

Controller	$\mathbf{p}_{p,xy}$ [cm]	ϕ_p [°]	ϑ_p [°]	$\boldsymbol{\theta}_l$ [°]	$\hat{f}_{p_z,e}$ [N]
PD	6.4	10.7	8.0	13.6	1.1
PD+C	6.3	9.2	6.9	12.0	0.9
Impedance	4.4	5.3	4.9	5.1	1.0

5.3 Experiment II: hovering in presence of external winds

In this experiment, the FPR was flown to hover in front of a wind generator placed along the x axis of the global frame during 60 s, with wind speed measured about 26 km/h. The platform is initially placed with zero yaw relative to the global frame, and thus the winds will perturb the tracking of leg angles and generate an external wrench on the platform mainly composed of: 1) an x-axis force expressed in the global frame; 2) a moment around negative y axis of the platform frame.

We then performed the above-mentioned hovering flights with different impedance gains on the platform's position and orientation states, while keeping the same gains for the additional DoFs of the leg angles. Fig. 5 shows the results of impedance controllers with varied mass and stiffness coefficients (higher or lower than the original values), and the damping coefficients being calculated to maintain the same damping ratio as given in Table 1. We found in the experiments that keeping the pre-determined damping ratio for all the states is crucial to a stable behavior of the robot especially in presence of external perturbations.

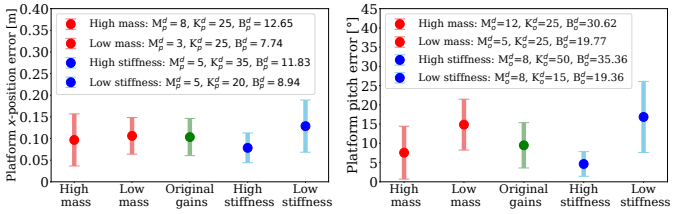

Fig. 5. Tracking error distribution of the platform x position and pitch angle ϑ_p with different impedance gains in Experiment II. Note that the tracking error is computed by the absolute value of the difference between the actual and desired states.

From the results, we can analyse and compare the different compliance behavior according to the variations in mass and stiffness coefficients. A higher value in mass coefficient might be beneficial to resist the external wrench (as shown in platform pitch response). However, the robot becomes less reactive to the external effects, which is unexpected during the interaction tasks. A proper value for the mass coefficient (as in the original gains) coherent with the mechanical and structural properties of the robot is preferable. On the other hand, a stiffer impedance system is always advantageous in rejecting the disturbances as shown in both cases. The concern of increasing stiffness would be the loss of compliance to the external environment and the problems of overshooting and oscillation that might occur. Based on this analysis, we combine the original gains on the platform position and leg angles with stiffer gains on the platform orientation given in Fig. 5, in order to maintain good compliance of the platform with more resilience against perturbations on the platform orientation.

5.4 Experiment III: contact-based interaction tasks

In this experiment, we flew the FPR to accomplish contact-based interaction tasks which present potentially the similar challenges for industrial applications in real-world scenario. The platform of the FPR (with the attached cylinder-form end-effector) was controlled to interact with a 35×35 cm wooden board fixed in the middle of the flight arena, considered as an unknown object in the environment such as the surface of a ceiling. The board is hung by multiple tightly-stretched ropes and attached with a heavy payload above, assumed to be stiff enough to resist the interaction force.

During the interaction tasks, the exact position of the contact is not necessarily known. A predefined trajectory is sent to the FPR for taking off and reaching the possible interaction pose measured by the MOCAP. Then a human operator sends the desired contact force commands with

Fig. 6. Interaction tasks performed by the FPR in Experiment III. Left column figures demonstrate the pushing tasks with different orientations, right figure shows the configuration in Task 2 & 3.

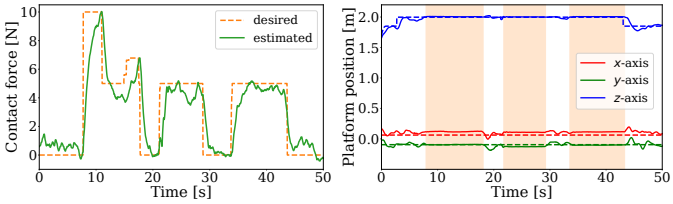

Fig. 7. Results for pushing with an inclined platform orientation in Task 1. Left graph shows the evolution of the desired and estimated contact force. Right graph presents the tracking of the platform position over the whole flight, with dashed lines representing the desired values. The orange shaded areas indicate the performed steady contacts.

Table 3. RMSE of the tracking of desired trajectories and contact force in Experiment III. Note that RMSE for $\mathbf{p}_p$ refers to the platform positioning errors, ϕ_p and ϑ_p is the platform roll and pitch angles, RMSE for $\boldsymbol{\theta}_l$ is the mean value of three leg angle errors and RMSE for ${}^p\mathrm{f}_{p_z,e}$ refers to the contact force errors.

Experiment	$\mathbf{p}_p$ [cm]	ϕ_p [°]	ϑ_p [°]	$\boldsymbol{\theta}_l$ [°]	${}^p\mathrm{f}_{p_z,e}$ [N]
Task 1 - Case 1	6.9	5.5	5.3	5.0	1.7
Task 1 - Case 2	7.9	6.5	6.7	4.3	1.5
Task 2	7.4	3.4	3.1	3.6	1.3
Task 3	10.3	2.7	6.1	4.7	1.0

a joystick. Several interaction tasks were performed with different configurations as shown in Fig. 6.

Task 1: pushing with different orientations

In the first task, the FPR was controlled to push the board by the platform in two different orientations: one in flat orientation and the other at an angle of about 10° in roll and 25° in pitch. Fig. 7 shows the results of the tracking of contact force and platform position for both cases. We remark that the estimated values of the contact force well track the desired values up to 10 N, validating the force tracking performance of the impedance controller. From the right graph in Fig. 7, we can well identify the steady contacts during which the platform position is further stabilized. The RMSE of the platform roll and pitch as well as the leg angles in Table 3 demonstrate that the robot configuration is stably controlled during the flight.

Task 2: pushing and twisting

In this task, the platform was controlled to interact with the board in flat orientation while twisting itself by yaw movement. When the contact is established, the operator sends both the desired contact force, yaw and yaw rate

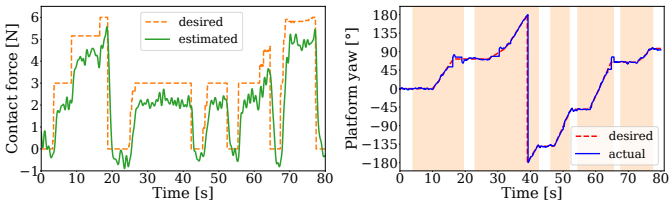

Fig. 8. Results for pushing & twisting task. Left graph presents the tracking of the desired contact force, and right graph plots the tracking of the platform yaw angle ψ_p.

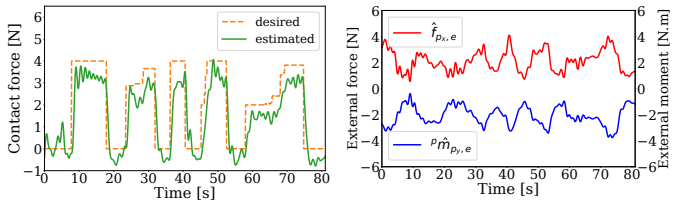

Fig. 9. Results for pushing task with external wind perturbations. Left graph demonstrates the tracking of the desired contact force. Right graph presents the x-axis external force estimate and y-axis external moment estimate on the platform.

commands. The pushing & twisting task was successfully accomplished according to the results shown in Fig. 8. The tracking of the desired contact force and the desired yaw of the platform was well performed. The other robot states are also stably controlled as shown in Table 3.

Task 3: pushing in presence of external winds

This task has involved a more challenging scenario where the FPR was performing the pushing task in presence of winds at a speed of about 13 km/h. The effects of the external winds are well estimated by the wrench estimator as shown in the upper right graph of Fig. 9, demonstrating a x-axis force of about 2 N and a negative pitch moment of about -2 N.m on the platform. The rest of the results shows that the interactions with the board were successfully achieved under the wind perturbations. The tracking of platform's x position and the pitch angle was perturbed, however the errors remain in reasonable range and the steady contacts have been performed.

All the interaction tasks were successfully accomplished, with acceptable RMSE on the tracking of the desired values given in Table 3. The desired contact forces are well tracked in all tasks, with tracking errors limited within 1.7 N. These results have shown the effectiveness of the implemented methods for performing interaction tasks.

6. CONCLUSION AND PERSPECTIVES

In this paper, we have implemented an impedance-based controller with an external wrench estimator for a Flying Parallel Robot interacting with the environment. The experimental results have demonstrated the FPR capable of rejecting disturbances and performing contact-based interactions in several configurations and external conditions. This work has thus shown the potential industrial applications that can be achieved by such aerial robots.

Future works may extend this work for more complex manipulation tasks, which are potentially achievable by a properly designed impedance behavior. A wrench analysis can be done to know about the feasible wrench exerted by the FPR in different robot configurations, which may be further applied to the planning of internal configuration (i.e. leg angles) to ensure optimal wrench feasibility of the robot based on a specific task. Finally, the estimation and control methods can be deployed in a decentralized manner as in Liu et al. (2021) using only onboard and intrinsic measurements, which will allow the FPR to perform manipulation tasks in fully unconstrained environments.

REFERENCES

Bodie, K., Brunner, M., Pantic, M., Walser, S., Pfndler, P., Angst, U., Siegwart, R., and Nieto, J. (2019). An Omnidirectional Aerial Manipulation Platform for Contact-Based Inspection. In *Proceedings of Robotics: Science and Systems*.

Brescianini, D., Hehn, M., and D'Andrea, R. (2013). Nonlinear Quadrocopter Attitude Control. Technical report, ETH Zurich.

Echeandia, S. and Wensing, P. (2021). Numerical Methods to Compute the Coriolis Matrix and Christoffel Symbols for Rigid-Body Systems. *Journal of Computational and Nonlinear Dynamics*, 16.

Li, Z., Song, X., Bégoc, V., Chriette, A., and Fantoni, I. (2021). Dynamic modeling and controller design of a novel aerial grasping robot. In *ROMANSY 23 - Robot Design, Dynamics and Control*, 538–546.

Liu, S., Erskine, J., Chriette, A., and Fantoni, I. (2021). Decentralized Control and Teleoperation of a Multi-UAV Parallel Robot Based on Intrinsic Measurements. In *2021 IEEE International Conference on Intelligent Robots and Systems (IROS)*, 6306–6312.

Michael, N., Fink, J., and Kumar, V. (2011). Cooperative manipulation and transportation with aerial robots. volume 30, 73–86. Springer.

Nguyen, H.N., Park, S., Park, J., and Lee, D. (2018). A Novel Robotic Platform for Aerial Manipulation Using Quadrotors as Rotating Thrust Generators. *IEEE Transactions on Robotics*, 34(2), 353–369.

Ollero, A., Tognon, M., Suarez, A., Lee, D., and Franchi, A. (2021). Past, Present, and Future of Aerial Robotic Manipulators. *IEEE Transactions on Robotics*, 1–20.

Ruggiero, F., Cacace, J., Sadeghian, H., and Lippiello, V. (2014). Impedance control of VToL UAVs with a momentum-based external generalized forces estimator. In *2014 IEEE International Conference on Robotics and Automation (ICRA)*, 2093–2099.

Ryll, M., Muscio, G., Pierri, F., Cataldi, E., Antonelli, G., Caccavale, F., Bicego, D., and Franchi, A. (2019). 6D interaction control with aerial robots: The flying end-effector paradigm. *The International Journal of Robotics Research*, 38(9), 1045–1062.

Sanalitro, D., Savino, H.J., Tognon, M., Cortés, J., and Franchi, A. (2020). Full-Pose Manipulation Control of a Cable-Suspended Load With Multiple UAVs Under Uncertainties. *IEEE Robotics and Automation Letters*, 5(2), 2185–2191.

Seraji, H. and Colbaugh, R. (1997). Force tracking in impedance control. *International Journal of Robotics Research*, 16(1), 97–117.

Shinners, S.M. (1998). *Modern control system theory and design*. John Wiley & Sons.

Six, D., Briot, S., Chriette, A., and Martinet, P. (2018). The Kinematics, Dynamics and Control of a Flying Parallel Robot with Three Quadrotors. *IEEE Robotics and Automation Letters*, 3(1), 559–566.

Tomić, T., Ott, C., and Haddadin, S. (2017). External Wrench Estimation, Collision Detection, and Reflex Reaction for Flying Robots. *IEEE Transactions on Robotics*, 33(6), 1467–1482.

Tzoumanikas, D., Graule, F., Yan, Q., Shah, D., Popovic, M., and Leutenegger, S. (2020). Aerial Manipulation Using Hybrid Force and Position NMPC Applied to Aerial Writing. In *Proceedings of Robotics: Science and Systems*.

Zhang, G., He, Y., Dai, B., Gu, F., Yang, L., Han, J., and Liu, G. (2019). Aerial grasping of an object in the strong wind: Robust control of an aerial manipulator. *Applied Sciences*, 9(11).